

Progressive Checkerboards for Autoregressive Multiscale Image Generation

David Eigen
de@deigen.net

Abstract

A key challenge in autoregressive image generation is to efficiently sample independent locations in parallel, while still modeling mutual dependencies with serial conditioning. Some recent works have addressed this by conditioning between scales in a multiscale pyramid. Others have looked at parallelizing samples in a single image using regular partitions or randomized orders. In this work we examine a flexible, fixed ordering based on *progressive checkerboards* for multiscale autoregressive image generation. Our ordering draws samples in parallel from evenly spaced regions at each scale, maintaining full balance in all levels of a quadtree subdivision at each step. This enables effective conditioning both between and within scales. Intriguingly, we find evidence that in our balanced setting, a wide range of scale-up factors lead to similar results, so long as the total number of serial steps is constant. On class-conditional ImageNet, our method achieves competitive performance compared to recent state-of-the-art autoregressive systems with like model capacity, using fewer sampling steps. Code is available at <https://github.com/deigen/checkerboardgen>.

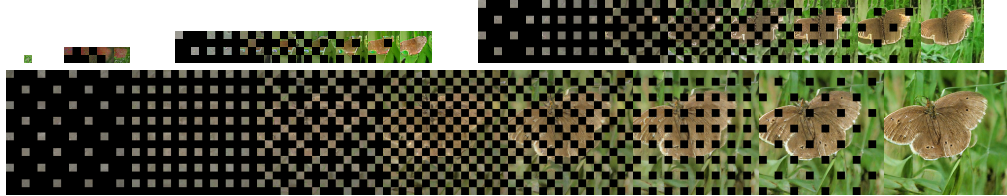


Figure 1: Progressive checkerboard samples from our model using 2x scale factor and 8 steps per scale. Masking applied to sampled locations at each step after decoding for visualization.

1 Introduction

Image generation methods, including autoregressive (AR) models, diffusion and masked models [24, 23, 29, 38, 32, 25, 9, 27, 2, 42], have shown impressive results in generating high-quality images. Recently, scalewise autoregressive models [37, 5, 18] condition from coarse to fine as their progressive sequence, while parallel AR models [40, 43] select multiple locations at once and condition using sequential blocks.

Both conditioning methods aim to model dependencies between sampling locations. Independently sampling mutually dependent locations can mix modes and produce incompatible values. This is particularly true for adjacent and nearby locations: if an image patch is red, the one next to it is likely to be red as well. Conditioning each location on a common parent, for example in the previous scale, makes the conditional samples more independent of each other [37].

Relying exclusively on scalewise conditioning, however, critically depends on a slow scale-up factor: If the scale factor is too large, then an object spanning multiple locations in one scale may not

yet be visible in the previous scale, so its appearance dependencies would not be conditioned and independently sampling can mix modes. Rather than scaling up by a factor of 2, as one might consider initially, the best performing multiscale models [37, 5, 18] currently scale by a factor of $\sqrt[3]{2} \approx 1.26$ (i.e. each factor of 2 is further subdivided into 3 evenly spaced scales). However, slow scale-up is not the only way to insert the necessary conditioning. As prior sequential and parallel methods [40, 43] have shown, another way is to condition between sampling locations.

In this paper, we examine conditioning between locations *within* each scale, making use of both between- and within-scale conditioning. We develop a sampling order based on a progressive checkerboard, which reduces mutual dependence within each sampling block and enables fast scale-up. Our ordering maintains balance at all levels in a quadtree subdivision, so that varying the block size effectively varies the trade-off between parallelism and modeling conditional dependencies. We use this to explore the relationships between scale-wise and within-scale conditioning, finding somewhat surprisingly that for this spatially balanced setup, the total number of sequential steps matters much more than the scaling factor. Our model’s performance is competitive with state-of-the-art methods in ImageNet 256x256 class-conditioned generation, using fewer sampling steps.

2 Related Work

2.1 Scalewise Autoregression

Gradual scaling AR models [37, 18, 5], first introduced by Tian et al. [37], progressively develop a full-resolution array of latent codes, which they use as a working “canvas” to apply residuals from each scale. At each iteration, the canvas is downsampled to the current scale (which grows by a factor of $\sqrt[3]{2}$ each iteration) and a transformer predicts residuals, which are upsampled and applied back to the full-resolution array.

The downsample-predict-upsample cycle implicitly invokes a progressive deblurring, similar to the progressive denoising of diffusion models. Since at each step the applied residuals are always upsampled from a smaller scale, they are blurry at full resolution, and the amount of blur decreases with each iteration as scales increase to the final resolution. Thus, the set of working values undergo a progressive deblurring in latent space.

Viewing the method this way sheds some light on reasons why the scaling factor remains small. Just as diffusion models struggle with large denoising steps due to their use of independent sampling and Gaussian noise [33, 31, 34, 17], scalewise AR models can struggle with large deblurring steps due to independently sampling underlying multi-modal distributions [1, 11].

2.2 Parallel Sampling

Parallel autoregression (PAR) by Wang et al. [40] generates images by sampling in parallel from equal-sized square partitions. Their method uses raster order within each partition and no multi-scale sampling, limiting its parallelism to only four groups. Our multi-scale checkerboard sampling uses both multi-scale and within-scale conditioning, as well as an efficient ordering that maintains sample balance and spatial diversity at all levels, reducing the number of sequential steps to just 17, while realizing further performance gains.

More recently, Zhang et al. [43] use a locality-aware ordering that adds far-away locations while simultaneously growing already-selected regions with adjacent samples, while Pang et al. [19] use random orderings. However, the former uses a more complex dynamic evolution to grow out regions, while both methods require additional position probe tokens, extending the overall sequence length. We use a simple but effective regular pattern combined with multiscale conditioning, and do not require additional probe tokens.

Yan et al. [41] use a two-stage “generation then reconstruction” approach applied in the context of MAR [15] that restricts the unmasking schedule to far-away locations using striations, the final stage of which corresponds to a mod 2 checkerboard. In contrast to their method, we use a fully balanced progressive checkerboard for all steps, along with explicit multiscale conditioning, in the context of direct autoregression instead of masking. Additional recent works include NAR [6], which uses different decoder heads for horizontal and vertical conditioning, leading to a striation pattern, and ARPG [14], which uses cross-attention for conditioning in random-ordered parallel sampling with masked models.

Some gradual scaling models also incorporate ways to reduce same-scale dependencies, though to a lesser extent. Han et al. [5] use random bit flips (“bitwise self-correction”) to address errors from independent sampling at the quantizer bit level after incorporating BSQ [44] as their tokenizer. Ma et al. [18] use a miniature masked image model applied in the autoregressor head to condition lower-confidence locations on higher-confidence ones. Somewhat further afield, to enable 2x scaling factors, Ren et al. [26] stack a flow-matching diffusion model on top of mixed-mode AR samples to resolve interdependences. Kutscher et al. [12] examine the impact of patch ordering in the context of recognition models.

3 Method

3.1 Autoregressor

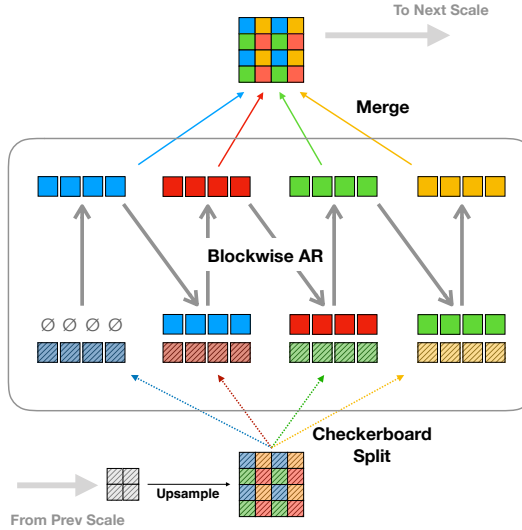


Figure 2: Overview of our multiscale blockwise checkerboard autoregressor. (For illustration there are $P = 4$ checkerboard blocks, while our actual model uses $P = 8$ for more spatial distancing.)

Our multiscale progressive checkerboard autoregressive model is built around a transformer [39, 21, 22] with blockwise causal mask using successive checkerboard sampling blocks.

Figure 2 provides an overview of our method. At each scale s , latent codes output by the previous scale $s - 1$ are upsampled by a scaling factor r to form the scalewise-conditioning input, $z_{s-1}^{up} = \text{upsample}(z_{s-1}, r)$. The locations of this map are split according to the progressive checkerboard ordering (see Sec. 3.2) into P blocks, $b_s^1, b_s^2, \dots, b_s^P$, where each block b_s^i contains $H_s W_s / P$ tokens. We randomize P during training to allow different degrees of parallelism at inference time.

In order for each autoregressive step to condition on previously sampled tokens *within* each scale, we include the output of each block into the input of later ones. In particular, we use a linear combination between the upsampled values z_{s-1}^{up} from the previous scale and the (shifted) outputs z_s of the current scale, along with learned position embeddings pos at both locations. The input tokens to the transformer are then

$$\text{inputs}(s, i) = W_{proj} \cdot \text{Concat}(z_{s-1}^{up}[b_s^i], z_s[b_s^{i-1}], pos[b_s^i], pos[b_s^{i-1}]) \quad (1)$$

where W_{proj} is a learned linear projection, and $[.]$ indicates indexing at the specified block locations. Since the first block b_s^1 has no previous block, we use learned constant vectors for $z_s[b_s^0]$ and $pos[b_s^0]$.

At inference, each block b_s^i contains the set of locations for each sampling step. Tokens are processed in parallel within each block, while the blocks themselves are serialized and sampled sequentially. Output tokens for each block are sampled independently using a multinomial.

During training, the entire sequence is processed in parallel using the ground truth codes z_s for both inputs and targets in a parallel autoregressive fashion. We use a blockwise causal mask, where all

tokens within each block b_s^i can attend to each other, as well as to tokens from all previous blocks, both for the same scale and in lower-resolution scales. Each token position outputs softmax logits for a quantized codebook; we use flat mean cross-entropy loss over all scales and positions.

Importantly, the locations in each block are spaced as evenly as possible. The number of locations that can be sampled in parallel depends on the independence between locations, when conditioned both on the previous scale and previous samples. Thus, there is a trade-off between the number of scales and the degree of parallelism within each scale, a relation that we explore later in Sec 4.3.

3.2 Progressive Scan Order

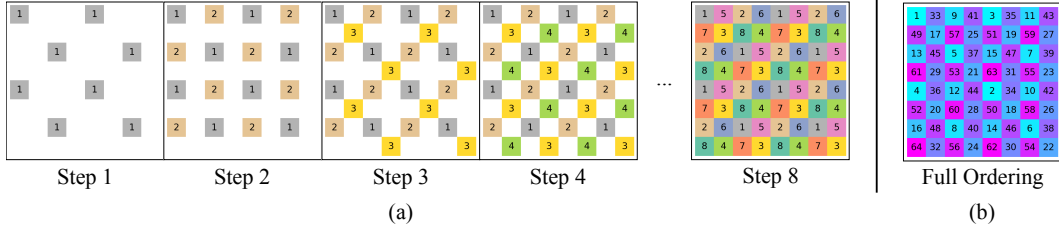


Figure 3: (a) Progressive checkerboard on an 8×8 grid using $P = 8$ steps. (b) Full ordering.

Algorithm 1 Progressive Checkerboard Scan Order

```
def ProgressiveCheckerboard(size, x=0, y=0):
    if size == 1: return [(x, y)]
    d = size // 2
    # create balanced lists for TL, BR, TR, BL
    sublists = [
        ProgressiveCheckerboard(d, xi, yi)
        for (xi, yi) in ((x,y), (x+d,y+d), (x+d,y), (x,y+d))
    ]
    # combine round-robin from the quadrants
    return concat(zip(*sublists))
```

To create the progressive checkerboard ordering, we use a balanced quadtree index generator, where the 2D grid of size $N \times N$ is recursively subdivided into quadrants and indices are assigned in such a way as to maintain balanced assignment at all quadtree levels.

We use a divide-and-conquer approach, where at each recursion level, balanced index lists are first generated for each quadrant recursively, then merged using round-robin selection with a diagonal skip-step pattern (i.e., TL, BR, TR, BL). This results in a spatially balanced progressive order, with a unique index in $1 \dots N^2$ assigned to each of the $N \times N$ spatial positions. See Algorithm 1.

This scan order can be used flexibly with various partition sizes. To create the blocks b_s^i for each scale s , we simply divide the progressive scan order into P contiguous segments of equal size. If the grid size N is not a power of 2 (as is the case in our scaling experiments), we generate the order on the next power of 2 and restrict to the grid size. Figure 3 shows an example progressive checkerboard ordering on an 8×8 grid.

3.3 Token Embeddings

For token embeddings, we use quantized latent codes from a VAE-based autoencoder [24, 27, 13, 4]. Each scale is encoded separately from the RGB image, so that each scale's latents are directly interpretable and decodable. For transformer inputs, we pass the VAE latent codes through a small MLP to unfold them from their low-dimensional clustering space back to higher dimension. For outputs, we also tried using the cluster vectors in an MLP mapping to the weights of the linear output head; however, we found no benefit compared to ordinary linear head based on the code indices.

As described in section 3.1, for inputs, we linearly combine the upsampled latents from the previous scale with the shifted outputs from the current scale. This allows the transformer to condition on both sources of information in a pipelined fashion. In addition, we use a class token as the first input, which along with AdaLN [20] is used to condition on class labels with classifier-free guidance [10].

3.4 Position Encodings and RoPE Mixing

To make use of our blockwise checkerboard order’s ability to model local dependencies via sequential sampling, the transformer must be able to identify and attend to adjacent locations for each token. We accomplish this using both input position embeddings and learned rotary position encodings (RoPE) [35, 7] in self-attention layers.

We initialize RoPE encodings using factored space and scale frequency representations (7/8 spatial, 1/8 scale). Note the embeddings encode the position in the image-scale space, not the sampling order. The embeddings are then learned in the joint space, allowing the model to find a high-frequency adjacent-position basis and other attention patterns optimized for our sampling order.

Note each token in the transformer processes inputs from two locations: one for the current sampling positions b_s^i , and one for conditioning latents at the previous block’s positions b_s^{i-1} (Sec. 3.1). Eq. (1) supplies both in the linear mixture for the input layer. However, without modification, the attention layers only use RoPEs for the current positions b_s^i . To incorporate both sets of positions, we looked at mixing RoPEs for the attention keys using learned mixing coefficients¹ α_{lh} for each transformer layer l and attention head h :

$$rope_{lh}(b_s^i) = \alpha_{lh} \cdot rope(b_s^i) + (1 - \alpha_{lh}) \cdot rope(b_s^{i-1}),$$

where $rope(\cdot)$ produces RoPE embeddings for specified locations. Mixing is only applied to keys; queries always use the positions b_s^i , corresponding to the current sampling locations whose output is being computed. Although we did not see any performance gains with this strategy, we examine its behavior in Sec. 4.4, finding that only the first two layers use the previous block’s RoPE shifts. This indicates that conditional information is extracted early on, so input mixing is sufficient.

4 Experiments

4.1 Model and Training Details

We train our models on ImageNet [28] at 256x256 resolution. We experiment with two model sizes: the small (S) model has 12 transformer layers with hidden dimension 512 and 16 attention heads, while the large (L) model has 20 layers with hidden dimension 1024 and 16 heads. In most ablation experiments we use the S model size, trained for 100 epochs with a batch size of 128 and learning rate 1×10^{-4} , then dropped to 1×10^{-5} in two steps over 10 epochs. The L model is trained for 200 epochs with batch size 64 and learning rate 5×10^{-5} , then dropped to 1×10^{-5} for 5 epochs, followed by a second effective drop by increasing batch size to 320 via gradient accumulation for the last 5 epochs. In all cases, we use AdamW [16] optimizer with weight decay 0.01 and ten-crop transforms, running on a single NVIDIA GH200 GPU.

We use the VAE autoencoder from LlamaGen [36], with a codebook size of 4096. To better represent the smaller image sizes in our multiscale setting, we fine-tune by freezing all layers other than the quantizer codebook itself, and retrain the codebook layer on ImageNet for one epoch with random image sizes between 16 and 256, using an L2 loss on the latent codes before and after quantization.

To measure sample quality, we use Frechet Inception Distance (FID) [8] and Inception Score (IS) [30], computed using 50k samples against the full ImageNet validation set using the TensorFlow implementation from [36, 3].

For classifier-free guidance (CFG), we found applying CFG too early in the sampling progression limits sample diversity, likely due to the first samples’ influence on global structure. Because of this, we sample the first 5 steps (corresponding to the 1x1 and 2x2 scales when scaling by 2x) with CFG=0, and apply CFG for all subsequent steps. Following common practice [40, 6, 43], we perform a sweep of CFG values at 0.1 increments.

4.2 Benchmark Comparison

Table 1 compares our method against recent autoregression-based image generation models of similar model size on ImageNet 256x256. We show results for our Checkerboard-L model with a 2x scaling ratio and 4 sampling steps per scale (17 total), as well as a 4x ratio with 8 steps per scale (also 17

¹We learn the “logits” α' of the mixing coefficients and set $\alpha_{lh} = \text{sigmoid}(\alpha'_{lh})$.

Model	Params	FID \downarrow	IS \uparrow	Pre. \uparrow	Rec. \uparrow	#Steps	Time (s)
LlamaGen-L [36]	343M	3.07	256.1	0.83	0.52	576	12.58
VAR-d16 [37]	310M	3.30	274.4	0.84	0.51	10	0.12
PAR-L-4x [40]	343M	3.76	218.9	0.84	0.50	147	3.38
RandAR-L [19]	343M	2.55	288.8	0.81	0.58	88	1.97
NAR-L [6]	372M	3.06	263.9	0.81	0.53	31	1.01
ARPG-L [14]	320M	2.30	297.7	0.82	0.56	32	0.58
LPD-L [43]	337M	2.40	284.5	0.81	0.57	20	0.28
Checkerboard-L 2x cfg=1.4 (Ours)	343M	2.72	302.5	0.81	0.56	17	0.52
Checkerboard-L 2x cfg=1.5 (Ours)	343M	2.83	318.2	0.82	0.57	17	0.52
Checkerboard-L 4x cfg=1.7 (Ours)	343M	2.79	311.5	0.80	0.57	17	0.52

Table 1: Autoregressive image generation models on ImageNet 256x256. Inference time measured for single image generation on A100.

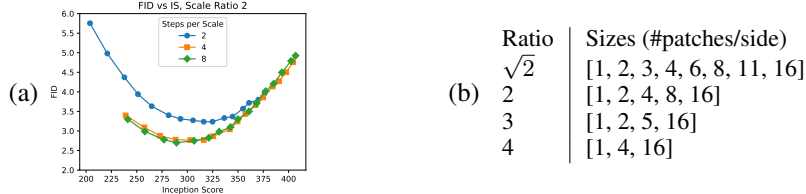


Figure 4: (a) FID vs IS computed at 0.1 CFG increments. L model size at 2, 4 and 8 steps per scale. (b) Exact scale sizes used in our experiments, for 256x256 image size and 16x16 VAE patch size.

total)². Compared to PAR [40] and RandAR [19], to which our method is most closely related, we achieve *similar or better FID and IS with fewer sampling steps and faster inference time*. While PAR uses 147 steps and RandAR 88 steps, we only need 17 steps to achieve a FID of 2.72 (compared to 3.76 and 2.55, respectively). Our inference time of 0.52s per image is also faster than both methods (3.38s for PAR and 1.97s for RandAR) on A100. In addition, our method is competitive with the more recent AR-based models ARPG [14] and LPD [43], notably also using fewer steps.

We show results for the full CFG sweep in Fig. 4(a) for our L model with different numbers of steps, and qualitative output samples in Fig. 8. While only 2 steps per scale is ineffective, both 4 and 8 perform similarly. In the next section, we explore the impact of number of steps in greater detail, and how these relate to the scaling ratio.

4.3 Relationship Between Scale Ratio and Sampling Steps

We explore the performance of our model for different multiscale scale factors and inference steps. Using the small (S) sized model, we train models using four scale-up factors: $\sqrt{2}$, 2, 3 and 4, as well as a single-scale baseline. The exact sizes are shown in Fig 4(b). We then evaluate each model using different numbers of sampling steps, varying the number of steps per scale, which corresponds to the partitioning size of the checkerboard pattern. Note that in our implementation, each scale ratio requires retraining, but the number of sampling steps can be varied at inference.

We evaluate each point using FID and IS with 50,000 samples, sweeping classifier-free guidance in 0.1 increments to obtain the best FID value for each setting. CFG is applied at all scales. To account for small variations in evaluation and sampling, for each point we record values with FID within 2% (relative) of its minimum, and plot the mean, min and max IS of these with error bars.

Figure 5 shows the results. On the left, we plot FID and IS by number of steps per scale, while on the right we plot them by total number of steps. While IS scores are similar between multiscale models and the single-scale baseline, all multiscale models outperform the single-scale baseline in terms of FID, with the best performance achieved at scale ratios 2, 3 and 4. As expected, larger scale-up factors require more steps per scale to achieve good performance (left-side figures).

²For the L models, the 2x model is trained from scratch for 200 epochs, and the 4x model is initialized with the 2x model weights and trained for 30 epochs.

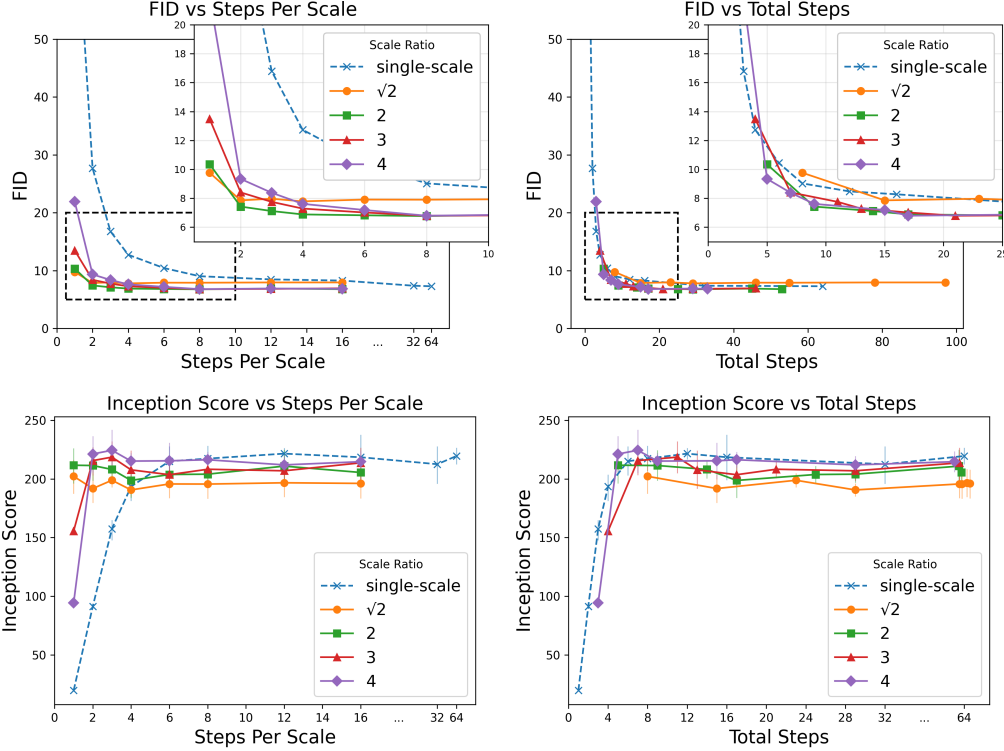


Figure 5: FID (top) and IS (bottom), by scale ratio and number of inference steps for the S model size. Left: by numbers of steps per scale; Right: by total number of steps. Multiscale models outperform the single-scale baseline. Note that scale ratios 2, 3 and 4 all achieve similar performance counted by *total steps*, even though the steps per scale needed to reach each total is different for each scale factor.

Notably, when viewed by the total number of steps (Fig. 5 top-right), scale ratios 2, 3 and 4 all achieve similar performance for each step count, *even though the steps per scale differ across scale factors*. The lines for these three ratios overlap tightly. However, all outperform the single-scale baseline as well as slower $\sqrt{2}$ scaling. This indicates that while multiscale conditioning is important, the exact scale factor is not very sensitive. Indeed, our checkerboard order also includes a degree of coarse-to-fine conditioning, simply due to its spatially balanced sampling, which may contribute to the insensitivity of the multiscale ratio. Thus *the total number of steps in the conditional chain is the dominant performance factor*.

Moreover, best performance is achieved at around 16 total steps for all of the multiscale models, while steps beyond this lead to little if any benefit. This makes sense, since partitioning our balanced checkerboard order into more steps spaces out the locations within each step, and coarse-to-fine conditioning is already included in the multiscale pyramid. Within-scale steps are needed largely to condition within the local upsampling windows. However, while between- and within-scale conditioning can model overlapping dependencies, we still find benefit to including both.

4.4 RoPE Mixing

As described in Sec. 3.3, we experimented with mixing RoPE embeddings for attention keys using learned mixing coefficients α_{lh} for each layer l and head h . Table 2(a) compares mixing for all layers, no layers, and only the first two layers. Training time increases when enabled for all layers, but is negligible when applied just to the first two. While we found no significant differences in FID or IS, the behavior of the mixing coefficients shown in 2(b) is illustrative of how the model uses sampling information in the inputs. Only the first two layers attend to sampled positions, indicated by negative weights. This suggests the model may extract information from the sampled locations early, possibly embedding it into representations at relevant output positions, and relying on attention based on output positions for most of the transformer. While this hypothesis is speculative, it is clear only the first layers use sampled positions, so including these in the input as in Eq. (1) is sufficient.

(a)

RoPE Mixing (S model size)		
	s/Batch	FID ↓
No Mixing	0.181	5.32
All Layers	0.195	5.33
First 2 Layers	0.184	5.46
		IS ↑
		234.7
		230.2
		226.5

(b)

Table 2: RoPE mixing strategies (see Sec. 3.3). (a) Results comparison; times use batch size 128 on single GH200. (b) Mixing weights when enabled for all layers. Negative weights (blue) correspond to sampled positions, while positive (red) correspond to output locations. Only the first two layers have negative weights: Information for previously-sampled values is extracted early.

4.5 Entropy Analysis

To further illustrate the behavior of multiscale checkerboard sampling, we plot measurements of entropy for the multinomial distribution at each token during sampling.

Fig. 6 shows aggregate measurements taken over 10,000 random samples of our L model. We show mean entropy as well as shaded regions corresponding to 25th and 75th percentiles, over each sampling step. As expected, entropy decreases as steps progress and samples resolve modes and variance by conditioning. Between scales, though, there is a jump in entropy, as additional higher-resolution details are introduced, followed by continued decrease as sampling within the scale develops. Interestingly, on average, the largest entropy drop within each scale occurs half-way through the ordering, when every-other location has been filled.

Fig. 7 shows entropy for a few individual samples, both over steps, and over locations. Here, we see a trend consistent with the aggregate measures, but also substantial variation, since the token distribution depends heavily on the image content being generated. Additionally, the entropy maps clearly display checkerboard patterns, a result of our sampling order. This underscores our method’s ability to model local conditional dependencies, particularly between adjacent locations.

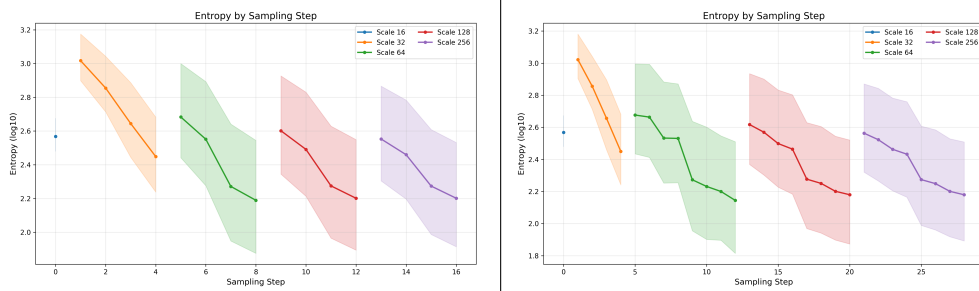


Figure 6: Aggregate entropy measurements over 10K samples. Entropy decreases within each scale, but jumps between scales as new details are introduced. Left: 4 steps/scale; Right: 8 steps/scale.

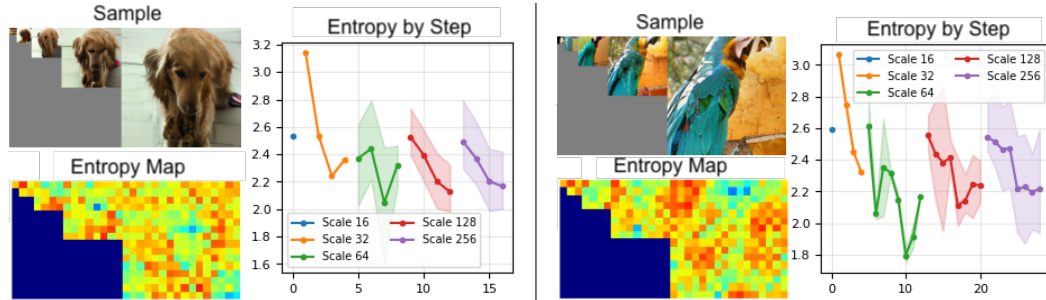


Figure 7: Entropy measurements for individual samples. Left: 4 steps/scale; Right: 8 steps/scale.

5 Conclusion

We have described a multiscale image generation method based on a spatially-balanced progressive checkerboard sampling order. By modeling both between-scale and within-scale conditional dependencies, our method is able to generate images with fewer sampling steps and competitive inference time compared to recent methods. Our experiments also show that in this setting, several multiscale pyramid ratios lead to similar performance for a given total number of sampling steps, enabling our method to use large scaling ratios of up to 4x. Future work may include extensions to video or text modalities, or further studying the relationship between scales and steps in the context of mutual information and dependency modeling.

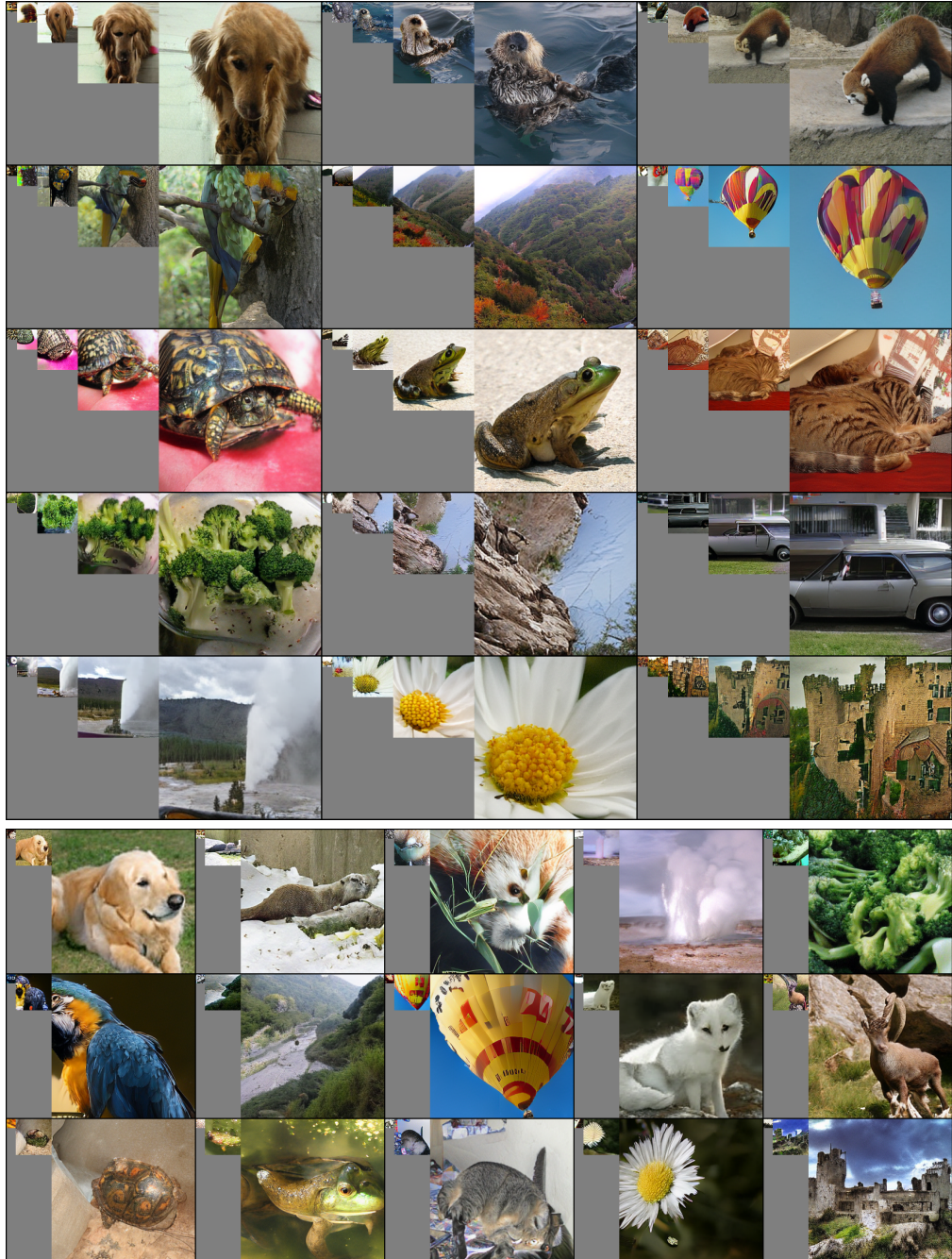


Figure 8: Samples from our Checkerboard-L model, scale factor 2x (top) and 4x (bottom).

References

- [1] Arpit Bansal, Eitan Borgnia, Hong-Min Chu, Jie S. Li, Hamid Kazemi, Furong Huang, Micah Goldblum, Jonas Geiping, and Tom Goldstein. Cold diffusion: Inverting arbitrary image transforms without noise. In *Advances in Neural Information Processing Systems*, 2023.
- [2] Huiwen Chang, Han Zhang, Jarred Barber, Aaron Maschinot, Jose Lezama, Lu Jiang, Ming-Hsuan Yang, Kevin Patrick Murphy, William T. Freeman, Michael Rubinstein, Yuanzhen Li, and Dilip Krishnan. Muse: Text-to-image generation via masked generative transformers. In Andreas Krause, Emma Brunskill, Kyunghyun Cho, Barbara Engelhardt, Sivan Sabato, and Jonathan Scarlett, editors, *Proceedings of the 40th International Conference on Machine Learning*, volume 202 of *Proceedings of Machine Learning Research*, pages 4055–4075. PMLR, 23–29 Jul 2023.
- [3] Prafulla Dhariwal and Alexander Nichol. Diffusion models beat gans on image synthesis. In *Advances in Neural Information Processing Systems*, volume 34, pages 8780–8794. Curran Associates, Inc., 2021.
- [4] Patrick Esser, Robin Rombach, and Bjorn Ommer. Taming transformers for high-resolution image synthesis. In *Proceedings of the IEEE/CVF Conference on Computer Vision and Pattern Recognition (CVPR)*, pages 12873–12883, June 2021.
- [5] Jian Han, Jinlai Liu, Yi Jiang, Bin Yan, Yuqi Zhang, Zehuan Yuan, Bingyue Peng, and Xiaobing Liu. Infinity: Scaling Bitwise AutoRegressive Modeling for High-Resolution Image Synthesis, June 2025. arXiv:2412.04431 [cs].
- [6] Yefei He, Yuanyu He, Shaoxuan He, Feng Chen, Hong Zhou, Kaipeng Zhang, and Bohan Zhuang. Neighboring Autoregressive Modeling for Efficient Visual Generation, March 2025. arXiv:2503.10696 [cs].
- [7] Byeongho Heo, Song Park, Dongyoon Han, and Sangdoo Yun. Rotary position embedding for vision transformer. In *European Conference on Computer Vision (ECCV)*, pages 289–305, 2024.
- [8] Martin Heusel, Hubert Ramsauer, Thomas Unterthiner, Bernhard Nessler, and Sepp Hochreiter. Gans trained by a two time-scale update rule converge to a local nash equilibrium. In *Advances in Neural Information Processing Systems*, volume 30, pages 6626–6637, 2017.
- [9] Jonathan Ho, Ajay Jain, and Pieter Abbeel. Denoising diffusion probabilistic models. In H. Larochelle, M. Ranzato, R. Hadsell, M.F. Balcan, and H. Lin, editors, *Advances in Neural Information Processing Systems*, volume 33, pages 6840–6851. Curran Associates, Inc., 2020.
- [10] Jonathan Ho and Tim Salimans. Classifier-Free Diffusion Guidance, July 2022. arXiv:2207.12598 [cs].
- [11] Emiel Hoogeboom and Tim Salimans. Blurring diffusion models, 2022.
- [12] Declan Kutscher, David M. Chan, Yutong Bai, Trevor Darrell, and Ritwik Gupta. Reordering patches improves vision models, October 2025. arXiv:2505.23751 [cs].
- [13] Anders Boesen Lindbo Larsen, Søren Kaae Sønderby, Hugo Larochelle, and Ole Winther. Autoencoding beyond pixels using a learned similarity metric. In Maria Florina Balcan and Kilian Q. Weinberger, editors, *Proceedings of The 33rd International Conference on Machine Learning*, volume 48 of *Proceedings of Machine Learning Research*, pages 1558–1566. PMLR, 20–22 Jun 2016.
- [14] Haopeng Li, Jinyue Yang, Guoqi Li, and Huan Wang. Autoregressive Image Generation with Randomized Parallel Decoding, September 2025. arXiv:2503.10568 [cs].
- [15] Tianhong Li, Yonglong Tian, He Li, Mingyang Deng, and Kaiming He. Autoregressive image generation without vector quantization. In *Advances in Neural Information Processing Systems*, 2024.
- [16] Ilya Loshchilov and Frank Hutter. Decoupled weight decay regularization. In *International Conference on Learning Representations (ICLR)*, 2019.
- [17] Cheng Lu, Yuhao Zhou, Fan Bao, Jianfei Chen, Chongxuan Li, and Jun Zhu. Dpm-solver: A fast ode solver for diffusion probabilistic model sampling in around 10 steps. In *Advances in Neural Information Processing Systems*, volume 35, pages 5775–5787, 2022.

[18] Xiaoxiao Ma, Mohan Zhou, Tao Liang, Yalong Bai, Tiejun Zhao, Biye Li, Huaian Chen, and Yi Jin. STAR: Scale-wise Text-conditioned AutoRegressive image generation, February 2025. arXiv:2406.10797 [cs].

[19] Ziqi Pang, Tianyuan Zhang, Fujun Luan, Yunze Man, Hao Tan, Kai Zhang, William T. Freeman, and Yu-Xiong Wang. RandAR: Decoder-only Autoregressive Visual Generation in Random Orders, July 2025. arXiv:2412.01827 [cs].

[20] William Peebles and Saining Xie. Scalable diffusion models with transformers. In *Proceedings of the IEEE/CVF International Conference on Computer Vision (ICCV)*, pages 4195–4205, October 2023.

[21] Alec Radford, Karthik Narasimhan, Tim Salimans, and Ilya Sutskever. Improving language understanding by generative pre-training. Technical report, OpenAI, 2018.

[22] Alec Radford, Jeffrey Wu, Rewon Child, David Luan, Dario Amodei, and Ilya Sutskever. Language models are unsupervised multitask learners. Technical report, OpenAI, 2019.

[23] Aditya Ramesh, Prafulla Dhariwal, Alex Nichol, Casey Chu, and Mark Chen. Hierarchical text-conditional image generation with clip latents, 2022.

[24] Aditya Ramesh, Mikhail Pavlov, Gabriel Goh, Scott Gray, Chelsea Voss, Alec Radford, Mark Chen, and Ilya Sutskever. Zero-shot text-to-image generation. In Marina Meila and Tong Zhang, editors, *Proceedings of the 38th International Conference on Machine Learning*, volume 139 of *Proceedings of Machine Learning Research*, pages 8821–8831. PMLR, 18–24 Jul 2021.

[25] Ali Razavi, Aäron van den Oord, and Oriol Vinyals. Generating diverse high-fidelity images with vq-vae-2. In *Advances in Neural Information Processing Systems*, pages 14837–14847, 2019.

[26] Sucheng Ren, Qihang Yu, Ju He, Xiaohui Shen, Alan Yuille, and Liang-Chieh Chen. FlowAR: Scale-wise Autoregressive Image Generation Meets Flow Matching. In *Proceedings of the 42nd International Conference on Machine Learning (ICML)*, 2025.

[27] Robin Rombach, Andreas Blattmann, Dominik Lorenz, Patrick Esser, and Björn Ommer. High-resolution image synthesis with latent diffusion models. In *Proceedings of the IEEE/CVF Conference on Computer Vision and Pattern Recognition (CVPR)*, pages 10684–10695, June 2022.

[28] Olga Russakovsky, Jia Deng, Hao Su, Jonathan Krause, Sanjeev Satheesh, Sean Ma, Zhiheng Huang, Andrej Karpathy, Aditya Khosla, Michael Bernstein, Alexander C. Berg, and Li Fei-Fei. ImageNet Large Scale Visual Recognition Challenge. *International Journal of Computer Vision (IJCV)*, 115(3):211–252, 2015.

[29] Chitwan Saharia, William Chan, Saurabh Saxena, Lala Li, Jay Whang, Emily L. Denton, Kamyar Ghasemipour, Raphael Gontijo Lopes, Burcu Karagol Ayan, Tim Salimans, Jonathan Ho, David J. Fleet, and Mohammad Norouzi. Photorealistic text-to-image diffusion models with deep language understanding. In *Advances in Neural Information Processing Systems*, 2022.

[30] Tim Salimans, Ian J. Goodfellow, Wojciech Zaremba, Vicki Cheung, Alec Radford, and Xi Chen. Improved techniques for training gans. In *Advances in Neural Information Processing Systems*, volume 29, pages 2226–2234, 2016.

[31] Tim Salimans and Jonathan Ho. Progressive distillation for fast sampling of diffusion models. In *International Conference on Learning Representations (ICLR)*, 2022.

[32] Tim Salimans, Andrej Karpathy, Xi Chen, and Diederik P. Kingma. Pixelcnn++: Improving the pixelcnn with discretized logistic mixture likelihood and other modifications. In *International Conference on Learning Representations (ICLR)*, 2017.

[33] Jiaming Song, Chenlin Meng, and Stefano Ermon. Denoising diffusion implicit models. In *International Conference on Learning Representations (ICLR)*, 2021.

[34] Yang Song, Prafulla Dhariwal, Mark Chen, and Ilya Sutskever. Consistency models. In *Proceedings of the 40th International Conference on Machine Learning*, volume 202 of *Proceedings of Machine Learning Research*, pages 32211–32252. PMLR, 2023.

[35] Jianlin Su, Yu Lu, Shengfeng Pan, Bo Wen, and Yunfeng Liu. Roformer: Enhanced transformer with rotary position embedding, 2021.

- [36] Peize Sun, Yi Jiang, Shoufa Chen, Shilong Zhang, Bingyue Peng, Ping Luo, and Zehuan Yuan. Autoregressive Model Beats Diffusion: Llama for Scalable Image Generation, June 2024. arXiv:2406.06525 [cs].
- [37] Keyu Tian, Yi Jiang, Zehuan Yuan, Bingyue Peng, and Liwei Wang. Visual autoregressive modeling: Scalable image generation via next-scale prediction. In *Advances in Neural Information Processing Systems*, 2024.
- [38] Aäron van den Oord, Nal Kalchbrenner, and Koray Kavukcuoglu. Pixel recurrent neural networks. In *Proceedings of the 33rd International Conference on Machine Learning*, volume 48 of *Proceedings of Machine Learning Research*, pages 1747–1756. PMLR, 2016.
- [39] Ashish Vaswani, Noam Shazeer, Niki Parmar, Jakob Uszkoreit, Llion Jones, Aidan N Gomez, Łukasz Kaiser, and Illia Polosukhin. Attention is all you need. *Advances in neural information processing systems*, 30, 2017.
- [40] Yuqing Wang, Shuhuai Ren, Zhijie Lin, Yujin Han, Haoyuan Guo, Zhenheng Yang, Difan Zou, Jiashi Feng, and Xihui Liu. Parallelized Autoregressive Visual Generation. In *Proceedings of the IEEE/CVF Conference on Computer Vision and Pattern Recognition (CVPR)*, pages 12955–12965, 2025.
- [41] Feihong Yan, Peiru Wang, Yao Zhu, Kaiyu Pang, Qingyan Wei, Huiqi Li, and Linfeng Zhang. Generation then reconstruction: Accelerating masked autoregressive models via two-stage sampling, October 2025. arXiv:2510.17171 [cs].
- [42] Lijun Yu, José Lezama, Nitesh B. Gundavarapu, Luca Versari, Kihyuk Sohn, David Minnen, Yong Cheng, Vighnesh Birodkar, Agrim Gupta, Xiuye Gu, Alexander G. Hauptmann, Boqing Gong, Ming-Hsuan Yang, Irfan Essa, David A. Ross, and Lu Jiang. Language model beats diffusion – tokenizer is key to visual generation. In *International Conference on Learning Representations (ICLR)*, 2024.
- [43] Zhuoyang Zhang, Luke J. Huang, Chengyue Wu, Shang Yang, Kelly Peng, Yao Lu, and Song Han. Locality-aware Parallel Decoding for Efficient Autoregressive Image Generation, July 2025. arXiv:2507.01957 [cs].
- [44] Yue Zhao, Yuanjun Xiong, and Philipp Krähenbühl. Image and video tokenization with binary spherical quantization. In *International Conference on Learning Representations (ICLR)*, 2025.